RSC Advances

ROYAL SOCIETY OF CHEMISTRY

www.rsc.org/advances

RSC Advances

ARTICLE

Synthesis of silicon-doped reduced graphene oxide and its applications in dye-sensitive solar cells and supercapacitors†

Zegao Wang,[abc] Yuanfu Chen,*[a] Pingjian Li,*[a] Jiarui He,[a] Wanli Zhang,[a] Zheng Guo,[c] Yanrong Li,[a] and Mingdong Dong[b]

Heteroatom-doping of graphene is of fundamental importance to enable a wide range of optoelectronic and energy storage devices while exploring their basic material properties. Herein, a facile and low-cost method is presented to synthesize the silicon-doped reduced graphene oxide (Si-rGO) via annealing treatment of triphenylsilane and graphene oxide. Compared to the pristine reduced graphene oxide (rGO), Si-rGO exhibits significant enhancement in electrocatalytic and electrochemical properties: when Si-rGO is used as metal-free electrocatalyst in counter electrodes in dye-sensitized solar cells (DSSCs), the conversion efficiency is increased by 29.6%; when Si-rGO is used as active electrode in supercapacitor, the specific capacity is increased by 48.5%. This suggests that silicon doping can effectively improve the electrocatalytic ability and electrochemical performance. It is promising for Si-rGO to be used as metal-free catalytic and active material.

1. Introduction

Graphene, a new two-dimensional nanomaterial, has attracted much attention due to its excellent properties and broad range of potential applications in energy conversion and storage, such as oxygen reduction reaction, lithium ion batteries, supercapacitors and dye-sensitized solar cells (DSSCs).[1-4] So far, both theoretical and experimental studies have demonstrated that doping heteroatoms into graphene could effectively improve its electronic and chemical properties.[5,6] Recently, various non-metal element doped graphene have been synthesized, including nitrogen,[7,8] boron,[9,10] fluorinate,[11,12] sulphur[13,14] or phosphorus[15,16] doped graphene, which exhibited excellent electrochemical performance in LIBs, supercapacitors and DSSCs, or good electrical properties in field-effect transistors.

Besides the heteroatom doping mentioned above, theoretic research shows that the silicon doping can remarkably modulate the electronic structure and improve its physical/chemical properties.[17-19] Chen and Niu demonstrated that silicon doped graphene could be an excellent candidate for metal-free sensors for the NO_2 detection by theoretical and experimental investigations.[20,21] Lv et al. reported that it can efficiently quench the fluorescence and enhance the Raman scattering of organic molecules.[22] Just recently, our group demonstrated that the doping silicon into CVD graphene film could increase the hole concentration, and has relative higher mobility compared to other doped graphene.[23] These investigations show that the silicon-doped graphene has various excellent properties, which will extend the applications of graphene-based materials. Furthermore, there are some reports about nitrogen-, boron- and/or sulfur doped or co-doped graphene for applications in DSSCs and supercapacitors.[24-26] However, to the best of our knowledge, the application of silicon-doped graphene as metal-free counter electrodes in DSSCs and as active electrode materials in supercapacitors has not been explored yet.

In this study, we propose a facile, low-cost and scalable thermal annealing method for the synthesis of silicon-doped reduced graphene oxide (Si-rGO) using graphene oxide (GO) and triphenylsilane ($C_{18}H_{15}Si$) as carbon and silicon sources, respectively. Compared to undoped rGO, when Si-rGO acted as efficient metal-free electrocatalyst in counter electrodes in DSSCs, it demonstrates remarkable catalytic activity in I^-/I_3^- redox reaction; when Si-rGO was employed as an active electrode material in supercapacitors, it exhibits significantly enhanced electrochemical properties compared to undoped rGO.

2. Experimental

[a]State Key Laboratory of Electronic Thin Films and Integrated Devices, University of Electronic Science and Technology of China, Chengdu 610054, P. R. China. E-mail: yfchen@uestc.edu.cn; lipingjian@uestc.edu.cn
[b]Interdisciplinary Nanoscience Center (iNANO), Aarhus University, DK-8000 Aarhus C, Denmark
[c]Department of Engineering, Aarhus University, DK-8000 Aarhus C, Denmark
†Electronic supplementary information (ESI) available: TGA, UV-vis and FTIR spectra of samples.

ARTICLE

RSC Advances

2.1 Synthesis of Si-rGO and rGO.

GO was synthesized from flake graphite by a modified Hummers method.[13,16] To synthesize Si-rGO, 1 g GO and 1 g triphenylsilane ($C_{18}H_{15}Si$) were firstly ultrasonically dispersed in 50 ml ethanol, and then spread onto an evaporating dish and dried, forming a uniform solid mixture. Then, the GO and triphenylsilane mixture was placed into a quartz tube and annealed at 300 ^oC for 30 min with 500 sccm Ar. Finally, the Si-rGO was obtained by collecting and washing several times. For comparison, the undoped rGO was synthesized by the same procedure except that the triphenylsilane was absent.

2.2 Fabrication of Si-rGO and rGO active electrode.

The Si-rGO (or rGO) counter electrodes (CEs) were fabricated as follows. Firstly, 90 wt% Si-rGO (or rGO) and 10 wt% polyvinylidene fluoride (PVDF) were dispersed in N-Methyl-2-pyrrolidone (NMP) by using an ultrasonic horn; then, the mixture was coated on fluorine-doped tin oxide glass plates to form counter electrode for DSSCs. Using the similar method, the mixture was coated on Ni foam to form active electrode for supercapacitor. The diameter of the Ni foam is 1.4 cm and the mass of the active material on each Ni foam is about 10 mg. All the active electrodes were heated in vacuum at 120 ^oC overnight.

2.3 Characterizations

The transmission electron microscopy (TEM) images were taken with an FEI Tecani G2 microscopy. The UV-vis and FTIR spectra of samples were performed on UV-1800 and NICOLET-460 FTIR spectrometer and thermal gravimetric analysis (TGA) tests were performed on TA Instruments Q50 with a heating rate of 20 ^oC/min in air. X-ray photoelectron spectroscopy (XPS) was performed on a Kratos XSAM800 using Al Ka radiation (144 W, 12 mA, 12 kV). The Raman spectra were performed by inVia Raman microscopy (Renishaw, 514 nm). The WiRE 4.1 software was used for Raman data acquisition and data analysis. The DSSC was made of a photoanode, a CE and a DHS-E23 electrolyte solution. The TiO_2 photoanode, N719 and DHS-E23 were purchased from Dalian Heptachroma SolarTech Co. Ltd.. The TiO_2 photoanode was sensitized by immersing into an ethanol solution containing the 0.5 mM N719 dye solution for 12 h. The photocurrent density-voltage characteristics of DSSCs were measured using a Keithley-2000 and Yokogaw-7651 source meters under the excitation of 100 mW/cm^2 AM 1.5 white light from a solar simulator. Cyclic voltammetry (CV) measurements were conducted, in which an as-prepared CE was taken as the working electrode in the two-electrode one-compartment cell and the Pt sheet was simultaneously served as both the reference electrode and counter electrode in an acetonitrile solution with 10 mM LiI, 1 mM I_2, and 0.1 M $LiClO_4$. The electrochemical impedance spectroscopy (EIS) measurements were performed in the frequency range of 0.1 Hz – 1 MHz in a two-electrode system on an electrochemical workstation (CHI660D, Chenhua Instruments Co., Shanghai, China). The CVs and galvanostatic charge/discharge experiments of supercapacitor were also performed on CHI660D in a two-electrode system. And the electrolyte was 5 M KOH solution. Specific capacitance determined by the galvanostatic charge/discharge was calculated using $C=2I/(dV/dt)$ with dV/dt is calculated from the slope of discharge curves, and I is the single electrode current density.

3. Results and discussion

The microstructure, morphology and element mapping of Si-rGO were investigated. Figure 1a shows a typical TEM image of Si-rGO. The image reveals transparent graphene sheets with wrinkle and fold features, which may originate from defective structures formed during the Si doping and reduction process of GO. Figure 1b is the SEM image of Si-rGO, which shows distinct crumpled structures and maintain the two dimensional geometry. As shown in Figure 1c, Si-rGO was further characterized by energy dispersive X-ray (EDX) spectrum, which confirms the presence of Si atoms. Figure 1d and 1e represents the EDX C and Si elemental mappings of Si-rGO, respectively. The uniform distribution of silicon suggests that the Si atoms are homogeneously distributed in graphene. In addition, thermal gravimetric analysis (TGA) tests in air were carried out on the samples, as shown in Fig. S1. As for GO, the sample exhibited two weight losses at onset temperatures of 208 and 550 ^oC, respectively. TGA also shows that the Si-doped samples undergo combustion at a slightly higher temperature than the pristine graphene.
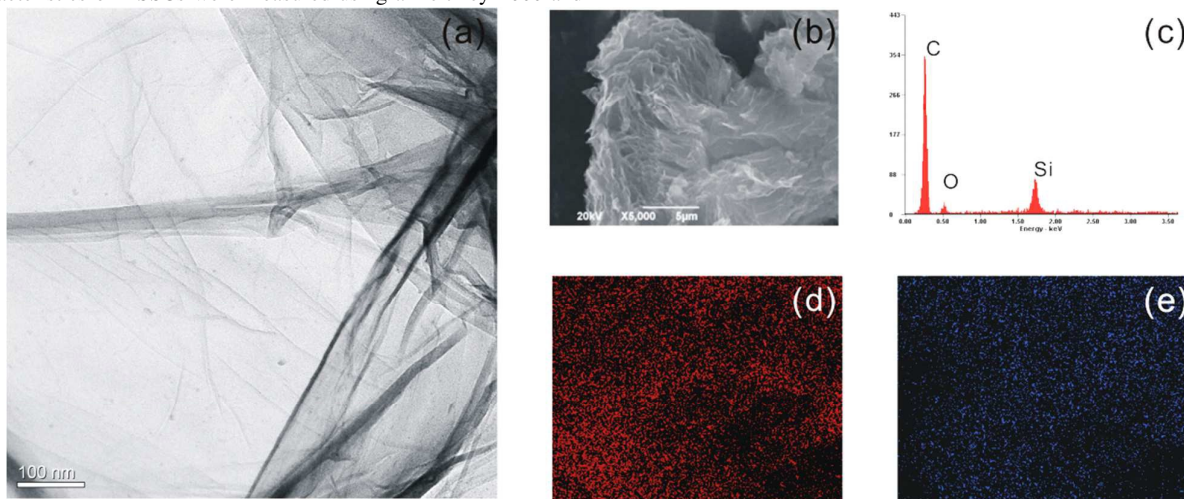
Fig. 1 TEM image of Si-rGO (a), SEM image (b) and EDX spectrum (c) of Si-rGO, C (d) and Si (e) EDX element maps of Si-rGO.

In order to further investigate the bonding configuration of Si atoms in Si-rGO, the XPS measurements were performed at room temperature. As shown in Figure 2, compared to GO, the Si 2s and 2p peaks appear and the intensity of O 1s peak decreases in the XPS spectrum of Si-rGO. It indicates that the Si atoms are incorporated into rGO and the large amounts of oxygen-functional groups on GO are removed during the annealing treatment. It is noted that the possibility of physical adsorption of Si onto the samples is excluded by the following reasons. The samples were ultrasonically dispersed in various solvents of ethanol, acetone, ether and H_2O; the XPS results reveal no change in the Si level before and after sonication. In addition, UV-vis and FTIR spectra of GO, rGO and Si-rGO were measured to confirm its reduction and shown in Fig. S2 and S3. The high-resolution Si 2p XPS spectrum of Si-rGO was then collected to gain more insight into silicon doping. As shown in Figure 2b, compared to rGO, there is an observable peak appearing in the range of 95~110 eV for Si-rGO, which originates from Si 2p. As for Si-rGO, the wider Si 2p XPS peak can be deconvoluted into three peaks at binding energies of

102.2, 103.0 and 103.9 eV, which correspond to the Si-C, C-Si-O and SiO_2 bonds, respectively. This is similar with other group's results.[21,22,27,28] By XPS elemental analysis, the total Si content (Si/C) in Si-rGO is 5.64 at%, in which Si-C/C, C-Si-O/C and SiO_2/C are 1.66, 2.39 and 1.59 %, respectively. Figure 2c shows the high-resolution C 1s spectrum of Si-rGO. The C 1s peak can be deconvoluted into four peaks at binding energies of ~ 284.7, 285.8, 287.5 and 289.9 eV, which correspond to C-C, C-O, C=O and O-C=O, respectively. In addition, the oxygen content (O/C) of rGO and Si-rGO are 15.4 and 11.3 at%, respectively. This indicates that the silicon doping preferentially occurs at the sites of oxygen functional groups and affords a more effective reduction of GO, which is similar to that of P and S doping and reduction of GO.[13,16] In addition, the effective reduction of GO will induce enhancement of carrier mobility of rGO.[13,29] Due to the low amount of Si atoms, Si-C was hardly observed in corresponding C 1s XPS spectrum, and it might be overlaid with C-C.[27,30] The XPS data strongly confirm that the silicon atoms are successfully incorporated into the graphene structure through a thermal annealing treatment.
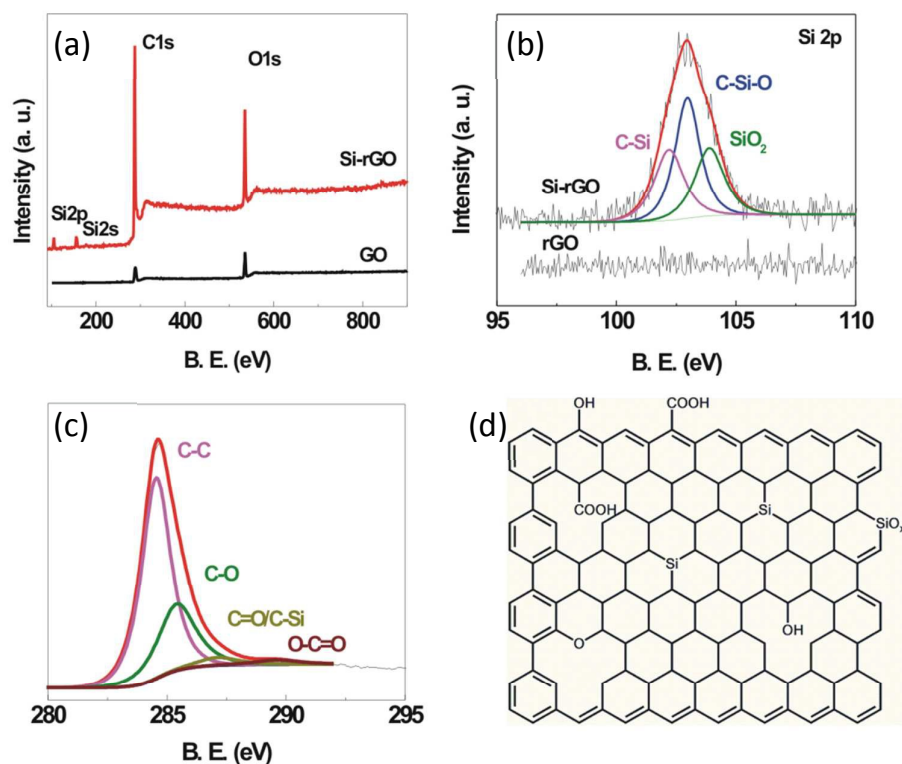
Fig. 2 XPS survey spectra of Si-rGO and GO (a), high resolution Si 2p spectra of Si-rGO and rGO (b), high resolution C 1s spectrum of Si-rGO (c) and the schematic structure of Si-rGO (d)[17-20].

Raman spectroscopy is an effective tool to investigate the doping effect of graphene. Figure 3 presents the Raman spectra of GO, rGO, and Si-rGO. All samples exhibit D-bands (~ 1350 cm^{-1}) and G-bands (~1580 cm^{-1}), which are usually assigned to structural disorder and the graphitized structure, respectively.[31]

Figure 3b shows corresponding I_D/I_G and the G-band position of such three samples. The intensity ratio I_D/I_G for the D-band and G-band is widely used for characterizing the defect quantity in graphene-based materials.[32] As shown in Figure 3b, compared to GO, the I_D/I_G of rGO and Si-rGO is higher, which

is attributed to the decreased sp^2 domains and the incomplete recovery of sp^3 defects after reduction.[33] The slight difference of rGO and Si-rGO may be related to the removal of the different functional groups upon reduction. The doped silicon atoms during reduction process also could affect I_D/I_G ratio.[8,23] On the other hand, the G-band corresponds to the first-order scattering of the E2g mode of sp^2 domain, and its position also corresponds to the change of carrier concentration with high sensitivity.[31,34] As seen from Figure 3b, compared to GO, the red shift (~2.0 cm^{-1}) the G-band of rGO was observed, which

can be attributed to the reduction of GO, and such a shift has been reported in both chemical and thermal reductions of GO.[11,35,36] Compared to rGO, the blue shift (~7.0 cm^{-1}) of the G-band in Raman spectra of Si-rGO was observed, which can be attributed to the silicon doping behaviour.[23] Niu group's and our group's previous results show the silicon doping in graphene exhibits p-type doping behavior.[21,23] Therefore, we can conclude that the blue shift of G-band reveals the increased hole concentration by silicon doping.

Fig. 3 Raman spectra of GO, rGO and Si-rGO (a) and the I_D/I_G of GO, rGO and Si-rGO (b).

Many reports have demonstrated that heteroatom doping can effectively improve the electrochemical properties of rGO; however, to the best of our knowledge, the application of Si-rGO as metal-free counter electrodes in dye-sensitized solar cells (DSSCs) has not been explored yet. Therefore, we prepare DSSCs where Si-rGO was employed as active material in counter electrode. To decrease the experiment error, each sample has been employed to prepare 5 counter electrodes to get the average value and error bars. CV and EIS measurements were performed to understand the reaction kinetics and electrocatalytic properties of rGO, Si-rGO and Pt, as shown in Figures 4a and 4b. It can be obviously observed one pair of reduction and oxidation peaks in all curves, which are attributed to the I_3^- reduction reaction and I$^-$ oxidation reaction, respectively.[16,37] As is known, the higher reduction current density corresponds to the faster rate for I_3^- reduction. As shown in Table 1, the I_3^- reduction peak current density ($I_{Reduction}$) is 0.87, 1.50 and 1.75 mA/cm^2, corresponding to rGO, Si-rGO and Pt, respectively. Figure 4b shows the EIS spectra, which is measured using DSH-23 as the electrolyte, and the equivalent circuit model used for fitting the resultant impedance spectra is illustrated in the inset of Figure 4b. The charge-transfer resistance (R_{ct}) is the resistance at the counter electrode/electrolyte interface for I_3^- reduction, and the lower R_{ct} means the higher electrocatalytic activity. As shown in Table 1, after doping silicon, the R_{ct} of rGO decrease from 9.37 to 5.42 Ω. This means that the Si-rGO counter electrode has higher electrocatalytic activity. Nevertheless, from Figure 4b, one can see that the solution resistance (Rs) of Si-rGO (~19.2 Ω) is much lower than that of rGO (~43.2 Ω). This is due to the lower resistance of Si-rGO, which is originating from higher carrier mobility and higher hole concentration, which are

confirmed with the XPS and Raman analysis. The CV and EIS measurements both show that Si-rGO can be used to realize I_3^- reduction, and its electrocatalytic activity is higher than that of rGO. Figure 4c shows the photovoltaic properties of DSSCs employing rGO, Si-rGO and Pt counter electrodes. From Table 1, one can see that after doping silicon, the short-circuit photocurrent density (I_{sc}) of DSSC increases from 11.66 to 12.06 mA/cm^2 and the fill factor (FF) increases from 46.20% to 57.81%; however, the open-circuit voltage (Voc) has almost no change. Compare to rGO counter electrode, the conversion efficiency of Si-rGO counter electrode increases from 3.82% to 4.95%, which is increased by 29.6%. Compared to Pt counter electrode, the conversion efficiency of Si-rGO is lower, which may be results from the lower I_3^- reduction peak current density and higher charge-transfer resistance.

In our previous study,[16] we reported the electrocatalytic of phosphorus-doped reduced graphene oxide (P-rGO) and the results were also shown in Table 1. Compared to P-rGO, Si-rGO has lower I_3^- reduction peak current density and higher charge-transfer resistance, and this leads to the conversion efficiency of Si-rGO is lower than that of P-rGO. This reveals that the enhanced ratio of electrocatalytic by doping silicon is lower than that of doping phosphorus, which may be due to the reduced barrier for I_3^- reduction, originating from the conjugation effect of the lone pair electrons on the phosphorus atoms and graphene π-system.[38-40] In addition, the doping configuration of silicon, such as Si-O-C, and the existence of SiO$_2$ nanoclusters will also give side effect on its properties. Nevertheless, compare to rGO, the Si-rGO has higher electrocatalytic properties, which demonstrates that doping silicon is also an effectively method to improve the electrocatalytic of rGO.

RSC Advances

ARTICLE
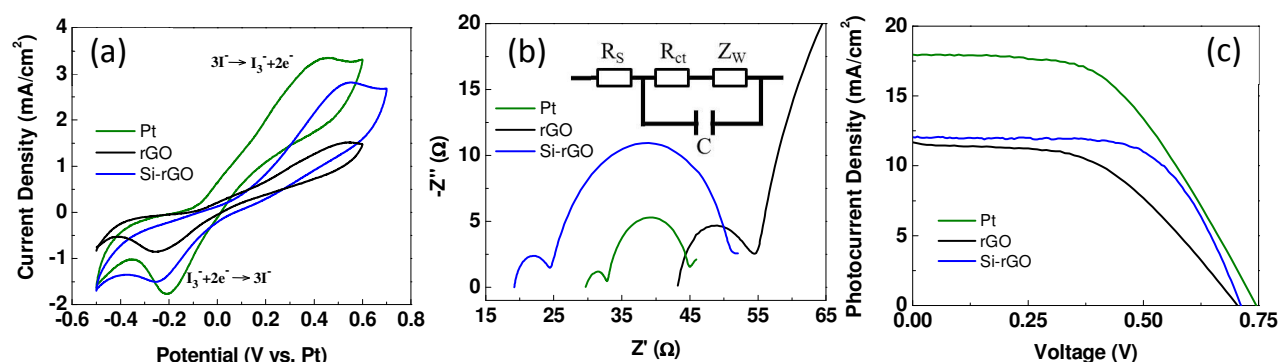
Fig. 4 The electrochemical properties of Si- rGO, rGO and Pt based counter electrodes, CV (a), EIS (b) and photovoltage vs photocurrent curves (c).

Table 1. The properties of rGO, Si- rGO, Pt and P-rGO counter electrodes

	$I_{Reduction}$ (mA/cm^2)	R_s (Ω)	R_{ct} (Ω)	I_{sc} (mA/cm^2)	V_{oc} (V)	FF (%)	η (%)
rGO	0.87±0.07	43.21±2.00	9.37±0.71	11.66±0.11	0.70±0.10	46.20±5.00	3.82±0.12
Si-rGO	1.50±0.06	19.28±2.10	5.42±1.01	12.06±0.15	0.71±0.10	57.81±4.00	4.95±0.14
Pt	1.75±0.05	29.61±1.50	3.21±0.65	17.95±0.11	0.74±0.10	51.65±4.00	6.86±0.12
P-rGO[16]	1.64±0.02	37.50±1.60	3.28±0.60	15.60±0.13	0.74±0.10	52.52±5.00	6.04±0.08

Furthermore, recent research shows that graphene-based double layer capacitors explore higher performance and is promising to be used in costumer electronic device.[41] Recently, nitrogen-, boron- or phosphorus doped graphene has been used to fabricate supercapacitor and all of them show higher performance compared with pristine graphene.[42,43] However, the use of silicon-doped graphene in supercapacitors has not been studied yet. A two-electrode system was first used to evaluate the electrochemical properties of Si-rGO. rGO was also tested using cyclic voltammograms techniques for comparison. Figures 5a and 5b show the CVs of rGO and Si-rGO in 5.0 M KOH solution at various scan rates. As for Si-rGO, there is no remarkable peak in all of the curves, and the rectangular CV curves indicate the ideal double layer capacitor feature with a charge/discharge process. But for rGO, as shown in Figure 5b, there is well-broadened peak in the range of 0.2-0.8 V, which indicates the presence of pseudo-capacitance.[44] This might be due to the higher oxygen content of rGO. Figure 5c shows the relationship between specific capacitance and current density, and the inset shows the galvanostatic charge/discharge curves of rGO and Si-rGO supercapacitors,

where the current density is 0.1 A/g. As seen, when the current density is 0.1 A/g, the specific capacitance of Si-rGO is 184.4 F/g, which is 48.5% larger than that of rGO (124.2 F/g). The specific power density can be obtained from equations as following: SP=E/Δt, while E could be calculated by E=CV^2/2, where the Δt is the discharge time. When the current density is 0.1 A/g, the specific power densities are 101 and 107 kW/kg, corresponding to rGO and Si-rGO. Further, when the current density increased to 5 A/g, the specific capacitance of Si-rGO is still higher than that of rGO. It is well known that the performance of carbon-based nanostructures for supercapacitors is highly dependent on both the nanostructure and the conductivity. The more pore/defect is thus significant for providing rich sites for adsorbing ions and accelerating electron transfer or decreasing electric resistance loss.[42,43,45] In this study, the silicon doping could break the basal plane of graphene and introduce more pore and also increase the concentration to enhance its conductivity. So we think that the higher specific capacitance is attributed to the more defect and the higher conductivity originating from silicon doping. Figure 5d is the EIS spectrum of rGO and Si-rGO, which are measured in KOH

solution. The electrode series resistance was derived from the high-frequency intersection of the Nyquist plot in the real axis. As seen, the series resistance of Si-rGO is lower than that of rGO, manifesting the low internal resistance of the Si-rGO. In low frequency region, both Si-rGO and rGO exhibited almost vertical line, indicating a nearly ideal capacitive behavior. Further, compare to rGO, the absence of the semicircle in Si-rGO demonstrated its high ionic conductivity at the electrode/electrolyte interface, which has also been observed in other reports.[46,47] The charge-transfer resistance could be noted by the intersections of the curves in the low frequency region, and they are 0.61 and 2.89 Ω for Si-rGO and rGO. The lower charge-transfer resistance of Si-rGO reveals that silicon doping could effectively facilitate the charge transfer process, which may be originating from higher conductivity and more defect after doping silicon.[47,48] The highly linear and symmetrical characteristic of charge/discharge curves, high specific capacitance of Si-rGO, make Si-rGO as a promising candidate in high-performance supercapacitors.
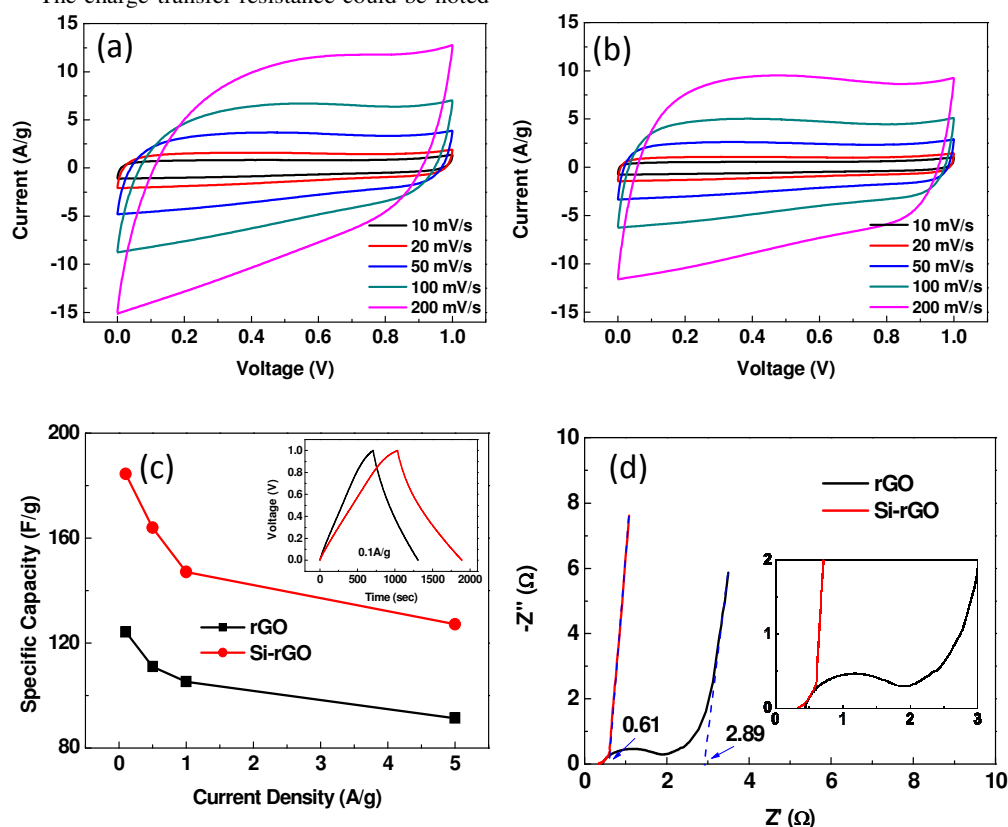
Fig. 5 The supercapcacitor properties of Si-rGO and rGO based electrode materials, CV curves at different scan rate of Si-rGO (a) and rGO (b), galvanostatic charge/discharge curves of Si-rGO and rGO (c) and the inset shows the specific capacity vs current density of Si-rGO and rGO, EIS spectrum of rGO and Si-rGO (d) and the inset shows its zoom-in plot.

4. Conclusions

In summary, silicon-doped rGO was synthesized by using graphene oxide and triphenylsilane as the carbon and silicon sources, respectively. HRTEM and EDS element mapping analysis show that the Si-rGO is few layer and the silicon atoms are uniformly distributed in the graphene sheet. XPS analysis reveals that the silicon doping content is about 5.64 at% and the silicon atoms are incorporated into the graphene lattice with Si-C, Si-C-O and SiO2 configurations. Raman study shows that the G-band will blue shift after doping silicon, which demonstrates that the hole concentration is increased. The Si-rGO was employed to fabricate the counter electrode in DSSCs, and the electrochemical measurement shows that the catalytic activity were improved after doping silicon and the conversion efficiency of Si-rGO based DSSCs increased by 29.6% compared to that of rGO. In addition, when Si-rGO was used to fabricate supercapacitors, its specific capacity is 184.4 F/g, which is 48.5% larger than that of undoped rGO (124.2 F/g). Si-rGO will extend the application of graphene in in optoelectronics and energy storage.

Acknowledgements

Notes and references

1 R. Raccichini, A. Varzi, S. Passerini and B. Scrosati, *Nat. Mater.*, 2015, **14**, 271-279.

2 J. L. Liu, M. H. Chen, L. L. Zhang, J. Jiang, J. X. Yan, Y. Z. Huang, J. Y. Lin, H. J. Fan and Z. X. Shen, *Nano Lett.*, 2014, **14**, 7180-7187.

3 Y. Y. Li, H. L. Zhu, F. Shen, J. Y. Wan, X. G. Han, J. Q. Dai, H. Q. Dai and L. B. Hu, *Adv. Funct. Mater.*, 2014, **24**, 7366-7372.

4 Z. G. Wang, P. J. Li, Y. F. Chen, X. Hao, J. B. Liu, R. Huang and Y. R. Li, *ACS Nano*, 2011, **5**, 7149-7154.

5 X. Wang, G. Sun, P. Routh, D. H. Kim, W. Huang and P. Chen, *Chem. Soc. Rev.*, 2014, **43**, 7067-7098.

6 D. S. Geng, N. Ding, T. S. Andy Hor, Z. L. Liu, X. L. Sun and Y. Zong, *J. Mater. Chem. A*, 2015, **3**, 1795-1810.

7 X. Wang, Q. H. Weng, X. Z. Liu, X. B. Wang, D. M. Tang, W. Tian, C. Zhang, W. Yi, D. Q. Liu, Y. Bando and D. Golberg, *Nano Lett.*, 2014, **14**, 1164-1171.

8 Z. G. Wang, P. J. Li, Y. F. Chen, J. B. Liu, H. J. Tian, J. H. Zhou, W. L. Zhang and Y. R. Li, *J. Mater. Chem. C.*, 2014, **2**, 7396-7401.

9 Z. H. Sheng, H. L. Gao, W. J. Bao, F. B. Wang and X. H. Xiu, *J. Mater. Chem.*, 2012, **22**, 390-395.

10 H. Wang, Y. Zhou, D. Wu, L. Liao, S. L. Zhao, H. L. Peng and Z. F. Liu, *Small*, 2013, **9**, 1316-1320.

11 K. Samanta, S. Some, Y. Kim, Y. Yoon, M. Min, S. M. Lee, Y. Park and H. Lee, *Chem. Commun.*, 2013, **49**, 8991.

12 K. Ho, C. H. Huang, J. H. Liao, W. J. Zhang, L. J. Li, C. S. Lai, C. Y. Su, *Sci. Rep.*, 2014, **4**, 5893.

13 Z. G. Wang, P. J. Li, Y. F. Chen, J. R. He, W. L. Zhang, O. G. Schmidt and Y. R. Li, *Nanoscale*, 2014, **6**, 7281-7287.

14 J. Zhang, J. J. Li, Z. L. Wang, X. N. Wang, W. Feng, W. Zheng, W. W. Cao and P. A. Hu, *Chem. Mater.*, 2014, **26**, 2460-2466.

15 S. Some, J .Kim, K. Lee, A. Kulkarni, Y. Yoon, S. Lee, T. Kim and H. Lee, *Adv. Mater.*, 2012, **24**, 5481-5486.

16 Z. G. Wang, P. J. Li, Y. F. Chen, J. R. He, J. B. Liu, W. L. Zhang and Y. R. Li, *J. Power Sources*, 2014, **263**, 246-251.

17 Y. G. Zhou, P. Yang, Z. G. Wang, H. Y. Xiao, X. T. Zu, X. Sun, M. A. Khaleel and F. Gao, *Appl. Phys. Lett.*, 2011, **98**, 093108.

18 D. Kaplan, V. Swaminathan, G. Recien, R. Balu and S. Krna, *J. Appl. Phys.*, 2013, **113**, 183701.

19 S. K. Mudedla, K. Balamurugan and V. Subramanian, *J. Phys. Chem. C*, 2014, **118**, 16165-16174.

20 Y. Chen, Y. J. Liu, H. X. Wang, J. X. Zhao, Q. H. Cai, X. Z. Wang and Y. H. Ding, *ACS Appl. Mater. Interfaces*, 2013, **5**, 5994-6000.

21 F. Niu, J. M. Liu, L. M. Tao, W. Wang and W. G. Song, *J. Mater. Chem. A.*, 2013, **1**, 6130-6133.

22 R. T. Lv, M. C. Dos Santos, C. Antonelli, S. M. Feng, K. Fujisawa, A. Berkdimer, R. Cruz-Silva, A. L. Elias, N. Perea-Lopez, F. Lopez-Urias, H. Terrones and M. Terrones, *Adv. Mater.*, 2014, **26**, 7593-7599.

23 Z. G. Wang, P. J. Li, Y. F. Chen, J. B. Liu, W. L. Zhang, Z. Guo, M. D. Dong and Y. R. Li, *J. Mater. Chem. C.*, 2015, **3**, 6301-6306.

24 K. F. Chen, S. Y. Song, F. Liu and D. F. Xue, *Chem. Soc. Rev.*, 2015, **44**, 6230-6257.

25 J. Han, L. L. Zhang, S. Lee, J. Oh, K. S. Lee, J. R. Potts, J. Y. Ji, X. Zhao, R. S. Ruoff and S. Park, *ACS Nano*, 2013, **7**, 19-26.

26 T. Wang, L. X. Wang, D. L. Wu, W. Xia and D. Z. Jia, *Sci. Rep.*, 2015, **5**, 9591.

27 K. Ueda, Y. Iijima, T. Maruyama and S. Naritsuka, *J. Nanosci. Nanotechnol.* 2010, **10**, 1.

28 E. Pippel, O. Lichtenberger and J. Woltersdorf, *J. Mater. Sci. Lett.*, 2000, **19**, 2059-2060.

29 Z. G. Wang, P. J. Li, Y. F. Chen, J. R. He, B. J. Zheng, J. B. Liu and F. Qi, *Mater. Lett.*, 2014, **116**, 416-419.

30 X. Hao, Y. F. Chen, Z. G. Wang, J. B. Liu and F. Qi, *Mater. Lett.*, 2014, **115**, 144-146.

31 A. C. Ferrari and D. M. Basko, Nat. Nanotechnol., 2013, 8, 235-246.

32 S. Abdolhosseinzadeh, H. Asgharzadeh and H. S. Kim, *Sci. Rep.*, 2015, **5**, 10160.

33 S. C. Lee, S. Some, S. W. Kim, S. J. Kim, J. Seo, J. Lee, T. Lee, J. H. Ahn, H. J. Choi and S. C. Jun, *Sci. Rep.*, 2015, **5**, 12306.

34 A. Das, S. Pisana, B. Chakraborty, S. Piscanec, S. K. Saha, U. V. Waghmare, K. S. Novoselov, H. R. Krishnamurthy, A. K. Geim, A. C. Ferrari and A. K. Sood, *Nat. Nanotechnol.*, 2008, **3**, 210-215.

35 Z. H. Ni, Y. Y. Wang, T. Yu and Z. X. Shen, *Nano Research*, 2008, **1**, 273-297.

36 G. Singh, D. S. Sutar, V. DIVAKAR Botcha, P. K. Narayanam, S. S. Talwar, R. S. Srinivasa and S. S. Major, *Nanotechnology*, 2013, **24**, 355704.

37 J. Ma, W. Shen, C. Li and F. Yu, *J. Mater. Chem. A.*, 2015, **3**, 12307-12313.

38 C. V. Rao, C. R. Cabrera, Y. Ishikawa, *J. Phys. Chem. Lett.*, 2010, **1**, 2622-2627.

39 T. Ikeda, M. Boero, S. Huang, K. Terakura, M. Oshima, J. Ozaki, *J. Phys. Chem. C*, 2008, **112**, 14706-14709.

40 R. A. Sidik, A. B. Anderson, N. P. Subramanian, S. M. Kumaraguru, B. N. Popov, *J. Phys. Chem. B*, 2006, **110**, 1787-1793.

41 Y. L. Shao, M. F. EI-Kady, L. J. Wang, Q. H. Zhang, Y. G. Li, H. Z. Wang, M. F. Mousavi and R. B. Kaner, *Chem. Soc. Rev.*, 2015, **44**, 3639-3665.

42 Z. S. Wu, A. Winter, L. Chen, Y. Sun, A. Turchanin, X. L. Feng and K. Mullen, *Adv. Mater.*, 2012, **24**, 5130-5135.

43 Y. Y. Wen, B. Wang, C. C. Huang, L. Z. Wang and D. Hulicova-Jurcakova, *Chem. Eur. J.*, 2015, **21**, 80-85.

44 B. Xu, S. F. Yue, Z. Y. Sui, X. T. Zhang, S. S. Hou, G. P. Cao and Y. S. Yang, *Energy Environ. Sci.*, 2011, **4**, 2826-2830.

45 Z. H. Wen, X. C. Wang, S. Mao, Z. Bo, H. Kim, S. M. Cui, G. H. Lu, X. L. Feng and J. H. Chen. Adv. Mater., 2012, 24, 5610-5616.

46 J. Y. Luo, H. D. Jang and J. X. Huang, *ACS Nano*, 2013, **7**, 1464-1471.

47 L. Wang, Y. J. Ye, X. P. Lu, Z. B. Wen, Z. Li, H. Q. Hou and Y. H. Song, *Sci. Rep.*, 2013, **3**, 3568.

48 E. Haque, M. M. Islam, E. Pourazadi, M. Hassan, S. N. Faisal, A. K. Roy, K. Konstantinov, A. T. Harris, A. I. Minett and V. G. Gomes. RSC Adv., 2015, 5, 30679-30686.

RSC Advances Accepted Manuscript